Simulation Study of ICRF Wave Propagation and Absorption in 3-D Magnetic Configurations

Tetsuya YAMAMOTO, Sadayoshi MURAKAMI and Atsushi FUKUYAMA

Department of Nuclear Engineering, Kyoto University, Kyoto 606-8501, Japan

(Received 28 November 2007 / Accepted 19 March 2008)

Ion cyclotron range of frequency (ICRF) wave propagation and absorption are investigated using TASK/WM, in which Maxwell's equation for an RF wave electric field with a complex frequency is solved as a boundary value problem. The wave propagation is solved in the tokamak (JT-60U) and helical (LHD) configurations in the minority ion heating regime. Magnetic flux coordinates based on the MHD equilibrium in LHD were obtained using the VMEC code. A new model for the radial extension of the magnetic coordinates is applied to improve the numerical error near the plasma-vacuum boundary. The ICRF wave propagation and absorption are clearly seen at the ion cyclotron resonance layer and two-ion-hybrid layers with a high spatial resolution.

Keywords: simulation, ICRF heating, wave propagation, helical configuration

DOI: 10.1585/pfr.3.S1075

1. Introduction

The ion cyclotron range of frequency (ICRF) heating experiments have been successfully performed, e.g., energetic ion production and long pulse plasma heating, and the efficiency of this heating method in LHD [1] has been determined. Comparisons of the experimental and numerical results are necessary to understand properties such as wave propagation, absorption, and evolution of velocity distribution function of ICRF heating in heliotrons. Numerical analyses of ICRF heating have been conducted using GNET [2]. The heating efficiency and detailed information about the energetic tail ion distribution were investigated in LHD. However, a simple RF wave electric field model was assumed, and a realistic RF wave field solution is necessary for this analysis.

In this study, we examine the ICRF wave propagation and absorption using TASK/WM [3–5], in which Maxwell's equation for the RF wave electric field with a complex frequency is solved as a boundary value problem in three dimensional (3D) magnetic configurations. A new model is applied to extend magnetic flux coordinates to the vacuum region based on the equilibrium data. This model improves the numerical error near the plasma-vacuum boundary. In addition, the analyses are conducted with a large scale computer for improving the special resolution, in order to observe the wave propagation and absorption in the ion cyclotron resonance and two- ion-hybrid layers in LHD clearly.

In section 2, we explain the simulation model used in TASK/WM. In section 3, we first describe the wave propagation and absorption in the tokamak configuration (JT-60U) to show the results in the axisymmetric configuration. Then, investigation of the helical configuration (LHD), where the minority ion heating regime is assumed, is presented. We consider the VMEC coordinates as the magnetic flux coordinates obtained from the MHD equilibrium in LHD.

author's e-mail: yamamoto@p-grp.nucleng.kyoto-u.ac.jp

2. Simulation Model

TASK/WM solves Maxwell's equation for the electric field, $\boldsymbol{E}$, with a complex frequency, ω, as a boundary value problem in a 3D magnetic configuration.

$$\nabla \times \nabla \times \boldsymbol{E} = \frac{\omega^2}{c^2} \overleftrightarrow{\epsilon} \cdot \boldsymbol{E} + i\omega\mu_0 \boldsymbol{j}_{\text{ext}} \tag{1}$$

Here, the external current, $\boldsymbol{j}_{\text{ext}}$, represents the antenna current density in ICRF heating. Assuming a cold plasma and a simple collisional dumping, the dielectric tensor is [6]

$$\overleftrightarrow{\epsilon} = \begin{pmatrix} S & -iD & 0 \\ iD & S & 0 \\ 0 & 0 & P \end{pmatrix},$$
$$S = 1 - \frac{1}{\epsilon_0} \sum_s \frac{\omega_{\mathrm{p}s}^2}{\omega} \frac{\omega + i\nu_s}{(\omega + i\nu_s)^2 - \Omega_s^2},$$
$$D = \frac{1}{\epsilon_0} \sum_s \frac{\omega_{\mathrm{p}s}^2}{\omega} \frac{\Omega_s}{(\omega + i\nu_s)^2 - \Omega_s^2},$$
$$P = 1 - \sum_s \frac{\omega_{\mathrm{p}s}^2}{\omega} \frac{1}{\omega + i\nu_s}, \tag{2}$$

where s and ϵ_0 are the particle species and dielectric constant in vacuum, and ν_s, $\omega_{\mathrm{p}s}$, and Ω_s are the collisionality, plasma frequency, and cyclotron frequency, respectively, for the s particle species.

We rewrite the Maxwell's equation (1) in magnetic coordinates (ψ, θ, φ). Left-hand side of Eq. (1) is written as

$$
\begin{aligned}
&(\nabla \times \nabla \times \boldsymbol{E})^p \\
&= \frac{1}{J}\left\{\frac{\partial}{\partial x^q}\left[\frac{g_{rp}}{J}\left(\frac{\partial E_r}{\partial x^q} - \frac{\partial E_q}{\partial x^r}\right) + \frac{g_{rq}}{J}\left(\frac{\partial E_p}{\partial x^r} - \frac{\partial E_r}{\partial x^p}\right)\right.\right. \\
&\quad \left. + \frac{g_{rr}}{J}\left(\frac{\partial E_q}{\partial x^p} - \frac{\partial E_p}{\partial x^q}\right)\right] - \frac{\partial}{\partial x^r}\left[\frac{g_{qp}}{J}\left(\frac{\partial E_r}{\partial x^q} - \frac{\partial E_q}{\partial x^r}\right)\right. \\
&\quad \left.\left. + \frac{g_{qq}}{J}\left(\frac{\partial E_p}{\partial x^r} - \frac{\partial E_r}{\partial x^p}\right) + \frac{g_{qr}}{J}\left(\frac{\partial E_q}{\partial x^p} - \frac{\partial E_p}{\partial x^q}\right)\right]\right\}, \qquad (3)
\end{aligned}
$$

where the metric coefficient $g_{ij} = \boldsymbol{e}_i \cdot \boldsymbol{e}_j$, $\boldsymbol{e}_i = \partial \boldsymbol{r}/\partial \boldsymbol{x}^i$ $(i, j, k = 1, 2, 3)$, and Jacobian J, $(x^1, x^2, x^3) = (\psi, \theta, \varphi)$. The indexes (p, q, r) are $(1, 2, 3)$, $(2, 3, 1)$, and $(3, 1, 2)$.

The dielectric tensor is written as

$$
\tilde{\epsilon}_{ij} = \overset{\leftrightarrow}{g}{}^{-1}_{ij} \cdot \overset{\leftrightarrow}{\mu}_{ij} \cdot \overset{\leftrightarrow}{\epsilon}_{ij} \cdot \overset{\leftrightarrow}{\mu}{}^{-1}_{ij}, \qquad (4)
$$

where the rotation transform tensor $\overset{\leftrightarrow}{\mu}$ is

$$
\begin{aligned}
\mu_{11} &= \frac{1}{\sqrt{g^{11}}}, \\
\mu_{12} &= \frac{1}{J\sqrt{g^{11}}}\left[\frac{B^\theta}{B}(g_{23}g_{12} - g_{22}g_{31}) \right. \\
&\quad \left. + \frac{B^\varphi}{B}(g_{33}g_{12} - g_{23}g_{31})\right], \\
\mu_{13} &= \frac{B^\theta}{B}g_{12} + \frac{B^\varphi}{B}g_{13}, \quad \mu_{21} = 0, \\
\mu_{22} &= \frac{B^\varphi}{B}J\sqrt{g^{11}}, \quad \mu_{23} = \frac{B^\theta}{B}g_{22} + \frac{B^\varphi}{B}g_{23}, \\
\mu_{31} &= 0, \quad \mu_{32} = -\frac{B^\theta}{B}J\sqrt{g^{11}}, \\
\mu_{33} &= \frac{B^\theta}{B}g_{32} + \frac{B^\varphi}{B}g_{33}. \qquad (5)
\end{aligned}
$$

The electric field $\boldsymbol{E}$ and metric coefficient g_{ij} are evaluated at the radial grid points ψ_l, and expanded to Fourier series in poloidal and toroidal directions.

$$
\begin{aligned}
\boldsymbol{E}(\psi_l, \theta, \varphi) &= \sum_{mn} \boldsymbol{E}_{mn}(\psi_l) e^{i(m\theta + n\varphi)}, \\
g_{ij}(\psi_l, \theta, \varphi) &= \sum_{m'n'} (g_{ij})_{m'n'}(\psi_l) e^{i(m'\theta + n'N_h\varphi)}, \qquad (6)
\end{aligned}
$$

where N_h is the pitch number of the helical coil in the toroidal direction, l is the radial mesh number, m is the poloidal mode number, and n is the toroidal mode number. The antenna current density $\boldsymbol{j}_{\rm ext}$ is given as

$$
\begin{aligned}
j^1 &= (j^1)_{mn} e^{i(m\theta + n\varphi)} \Theta(\psi - \psi_d), \\
j^{2,3} &= (j^{2,3})_{mn} e^{i(m\theta + n\varphi)} \delta(\psi - \psi_d), \qquad (7)
\end{aligned}
$$

where ψ_d is the radial antenna position and, $\Theta(x)$ and $\delta(x)$ are the step and delta functions, respectively. Eq. (7) satisfies $\nabla \cdot \boldsymbol{j}_{\rm ext} = 0$. In particular, we set up a system with two types of meshes that do not generally have equal distance in the ψ direction so that $\nabla \cdot (\nabla \times \boldsymbol{E}) = 0$ is satisfied. One is a mesh system that has ψ_l, l : *integer*, and the other is one that has $\psi_{l+1/2} = (\psi_l + \psi_{l+1})/2$. E_ψ component is defined at $\psi_{l+1/2}$, while E_θ and E_φ components are defined at ψ_l. Finally, the first (1) component of equation (3) is

$$
\begin{aligned}
&J(\nabla \times \nabla \times \boldsymbol{E})^1_{l-\frac{1}{2}} \\
&= \Big[-nl(G_{32})_{l-\frac{1}{2}} + lm(G_{33})_{l-\frac{1}{2}} \\
&\qquad + kn(G_{22})_{l-\frac{1}{2}} - km(G_{23})_{l-\frac{1}{2}}\Big] E_{\psi, l-\frac{1}{2}} \\
&+ \Big[\frac{1}{2}nl(G_{31})_{l-\frac{1}{2}} - \frac{1}{2}kn(G_{21})_{l-\frac{1}{2}} \\
&\qquad - il(G_{33})_{l-\frac{1}{2}}\frac{1}{\Delta_-} + ik(G_{23})_{l-\frac{1}{2}}\frac{1}{\Delta_-}\Big] E_{\theta, l-1} \\
&+ \Big[\frac{1}{2}nl(G_{31})_{l-\frac{1}{2}} - \frac{1}{2}kn(G_{21})_{l-\frac{1}{2}} \\
&\qquad + il(G_{33})_{l-\frac{1}{2}}\frac{1}{\Delta_-} - ik(G_{23})_{l-\frac{1}{2}}\frac{1}{\Delta_-}\Big] E_{\theta, l} \\
&+ \Big[-\frac{1}{2}ml(G_{31})_{l-\frac{1}{2}} + \frac{1}{2}mk(G_{21})_{l-\frac{1}{2}} \\
&\qquad + il(G_{32})_{l-\frac{1}{2}}\frac{1}{\Delta_-} - ik(G_{22})_{l-\frac{1}{2}}\frac{1}{\Delta_-}\Big] E_{\varphi, l-1} \\
&+ \Big[-\frac{1}{2}ml(G_{31})_{l-\frac{1}{2}} + \frac{1}{2}mk(G_{21})_{l-\frac{1}{2}} \\
&\qquad - il(G_{32})_{l-\frac{1}{2}}\frac{1}{\Delta_-} + ik(G_{22})_{l-\frac{1}{2}}\frac{1}{\Delta_-}\Big] E_{\varphi, l}, \qquad (8)
\end{aligned}
$$

where $k = n + n'N_h$, $l = m + m'$, and $G_{ij} = g_{ij}/J$.

Next, we consider the boundary conditions. We assume that the plasma is surrounded by a perfect conductor, and there exists a vacuum layer between the plasma surface and the perfect conductor wall. Then, the tangential electric field at the wall is set to zero at the boundary;

$$
E_\theta^{mn} = 0, \quad E_\varphi^{mn} = 0. \qquad (9)
$$

The poloidal electric field and toroidal electric fields of the $m \neq 0$ mode are zero at the magnetic axis, i.e., $\psi = 0$. In addition, the radial derivative of the toroidal electric field of the $m = 0$ mode is zero; i.e.,

$$
\left\{
\begin{array}{ll}
m = 0 & \partial E_\varphi^{0n}/\partial\psi\big|_{\psi=0} = 0 \\
m \neq 0 & E_\varphi^{mn}\big|_{\psi=0} = 0
\end{array}
\right. . \qquad (10)
$$

The Maxwell's equation (1) based on Eq. (8) is solved under the boundary conditions Eqs. (9) and (10) of the 3D magnetic configuration given by the numerical equilibrium data in the magnetic flux coordinates.

The numerical equilibrium determined using the VMEC code is used in TASK/WM. The VMEC code provides the physical quantities (magnetic field, magnetic flux, pressure, etc.) in the plasma inside the last closed flux surface. However, the physical quantities in the vacuum region are also necessary for solving the propagation of the waves excited by the antenna set outside the plasma. The first order extrapolation has been used to extrapolate the data from the plasma surface to the perfect conductor outside the plasma. In this case, the radial quantities changed discontinuously, which caused unphysical change in the wave propagation results. Therefore, we applied the second order extrapolation to improve wave propagation near the boundary.

A large scale analysis is conducted with the super computer SX-8 to improve the resolution of the simulation results. The simulation has been performed with $(l, m, n) = (100, 16, 4)$ (the memory size is about 1.4 GB), where, m, and n are same as in Eq. (6). In this study, we perform the simulation with $(l, m, n) = (100, 32, 8)$ (the memory size is about 9.5 GB).

3. Simulation Results

3.1 Tokamak configuration (JT-60U)

We first study ICRF minority heating in the tokamak configuration, taking JT-60U plasma as an example. The results are compared with those in the helical configuration in section 3.2. The assumed configuration parameters are as follows: the plasma major radius $R_0 = 3.5$ m the plasma minor radius $a = 0.98$ m the plasma shape elongation $\kappa = 1.3$ the plasma shape triangularity $\delta = 0.31$, and the magnetic field at magnetic axis $B_0 = 3.3$ T.

The typical results obtained using TASK/WM for the minority ion heating regime in the JT-60U configuration are shown in Fig. 1. We assume the following plasma parameters: the temperature at the magnetic axis $T_0 = 3.0$ keV and at the plasma boundary $T_s = 0.3$ keV, the density at the magnetic axis $n_0 = 1.0 \times 10^{20}\,\mathrm{m}^{-3}$ and at the plasma boundary $n_s = 0.1 \times 10^{20}\,\mathrm{m}^{-3}$, the minority ion ratio 5%, and the ratio of the collision frequency to the wave frequency $\nu_s = 0.003$. The temperature and density profiles are given by $T(r/a) = (T_0 - T_s)(1 - (r/a)^2) + T_s$ and $n(r/a) = (n_0 - n_s)(1 - (r/a)^2)^{1/2} + n_s$, respectively. We assumed the antenna current density $j_{\mathrm{ext}} = 1.0$ A/m, and the wave frequency $f_{\mathrm{RF}} = 45.0$ MHz.

The three lines in Fig. 1-(b) correspond to the ion cyclotron resonance layer, two-ion-hybrid cut-off layer, and two-ion-hybrid resonance layer outside the torus (right side). The dispersion relation is given by $N_x^2 = (R - N_z^2)(L - N_z^2)/(S - N_z^2)$ in a cold plasma; therefore, the expressions for these layers are as follows:

$$S = N_z^2 \quad \text{(Two-ion-hybrid resonance)}, \tag{11}$$

$$L = N_z^2 \quad \text{(Two-ion-hybrid cut-off)}, \tag{12}$$

$$R = N_z^2 \quad \text{(Two-ion-hybrid cut-off)}, \tag{13}$$

where N is the refractive index, $R = (S - D)/2$, and $L = (S - D)/2$.

In TASK/WM, the analysis for each toroidal wave mode number is conducted independently, and the final result is obtained by adding the results of many mode numbers. Figure 1 shows the results of adding $n_{\varphi 0} = 0$-39 ($n_{\varphi 0}$ is the center mode number of the toroidal wave mode number and $n = n_{\varphi 0}$ in Eq. (7) is the toroidal mode number of the waves exited by the antenna current). However, the superposed results show similar tendency as the results with the analysis using one toroidal mode. Therefore, in the following tokamak analyses, we performed the calculation with one toroidal mode number, $n_{\varphi 0} = 8$.

It is shown that the absorption region of minority ions is located near the minority ion cyclotron resonance layer in Fig. 1 (b). Coherent waves are observed in Figs. 1-(c) and (d). The Re E_+ component (left-circularly polarized component) of the electric field is absorbed, and the amplitude of coherent waves is damped near the minority ion cyclotron resonance layer (Fig. 1-(c)). On the other hand, the damping of the amplitude of the Re E_- component (right-circularly polarized component) is not observed near the minority ion cyclotron resonance layer. The reason is that the energy of the Re E_- component of the electric field is not absorbed by the minority ions in the ion cyclotron resonance layer if we assume cold plasma dispersion. The absorption increases at the two-ion-hybrid layers near the minority ion cyclotron resonance layer (Fig. 1-(a) and (b)). The expression of the absorption power $P(\psi, \theta, \varphi)$ is given by

$$P(\psi, \theta, \varphi) = \frac{1}{2}\mathrm{Re}\left[\boldsymbol{E}^* \cdot \left(-i\epsilon_0\omega(\overleftrightarrow{\epsilon} - \overleftrightarrow{I})\right) \cdot \boldsymbol{E}\right], \tag{14}$$

where $\boldsymbol{E}^*$ is a complex conjugate of $\boldsymbol{E}$, and $\overleftrightarrow{I}$ is the unit tensor. At the ion cyclotron resonance layer, the absorption rate due to the dielectric tensor $\overleftrightarrow{\epsilon}$ is high, but the amplitude

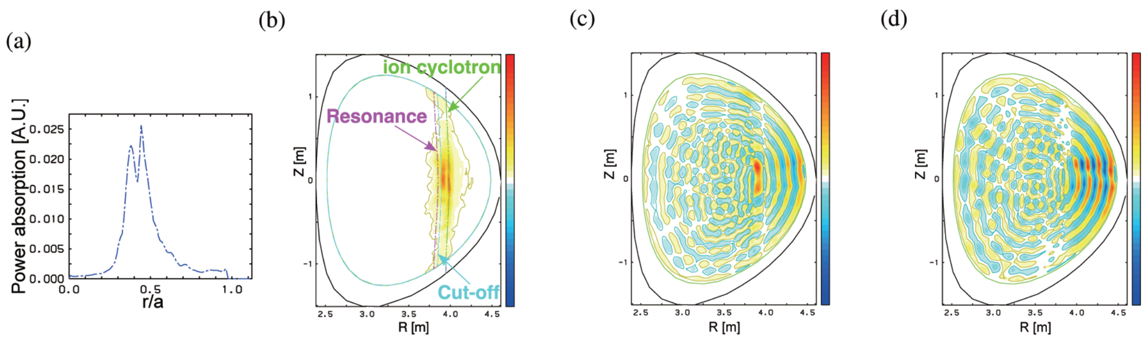

Fig. 1 Wave propagation and absorption in the minority heating regime of the JT-60U configuration: the minority ion absorption power as a function of the averaged minor radius (a), contour plots of minority ion absorption on the poloidal cross section (b), Re E_+ component of the RF electric field (c), and Re E_- component of the RF electric field (d). $f_{\mathrm{RF}} = 45.0$ MHz.

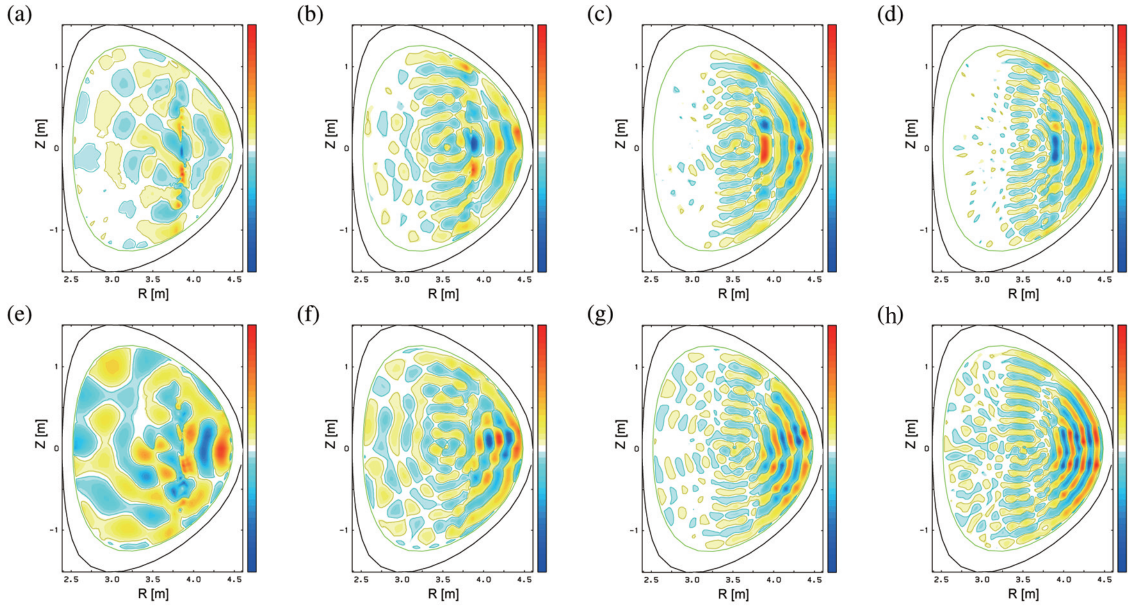

Fig. 2 Plasma density dependence of wave propagation in the minority heating regime of the JT-60U configuration: $n_0 = 0.1 \times 10^{20}\,\mathrm{m}^{-3}$ (a) and (e); $0.3 \times 10^{20}\,\mathrm{m}^{-3}$ (b) and (f) $0.5 \times 10^{20}\,\mathrm{m}^{-3}$ (c) and (g); and $0.7 \times 10^{20}\,\mathrm{m}^{-3}$ (d) and (h). Upper side: contour plots of $\mathrm{Re}\,E_+$ component of the RF electric field on the poloidal cross section and lower side: contour plots of $\mathrm{Re}\,E_-$ component of the RF wave electric field. $n_{\varphi 0} = 8$.

of the electric field is small. On the other hand, at the two-ion-hybrid layers, the absorption rate is low, but the amplitude of the electric field is large. These are the reasons for the absorption increase. Next, we study the plasma density dependence of the wave propagation and absorption in the JT-60U configuration.

Figure 2 shows the results with $n_{\varphi 0} = 8$ and varying density, $n_0 = 0.1 \times 10^{20}\,\mathrm{m}^{-3}$ (Figs. 2-(a) and (e)), $n_0 = 0.3\times10^{20}\,\mathrm{m}^{-3}$ (Figs. 2-(b) and (f)), $n_0 = 0.5\times10^{20}\,\mathrm{m}^{-3}$ (Figs. 2-(c) and (g)), and $n_0 = 0.7 \times 10^{20}\,\mathrm{m}^{-3}$ (Figs. 2-(d) and (h)). The other parameters are the same as in the case of Fig. 1. $\mathrm{Re}\,E_+$ and $\mathrm{Re}\,E_-$ components of the electric field are shown on the upper and lower sides, respectively, in Fig. 2. In the case of higher density n_0 ($n_0 = 0.5$ and $0.7 \times 10^{23}\,\mathrm{m}^{-3}$), coherent waves are observed (Figs. 2-(c), (d), (g), and (h)), while in the case of lower density ($n_0 = 0.1$ and $0.3 \times 10^{23}\,\mathrm{m}^{-3}$), coherent waves are not observed (Figs. 2-(a), (b), (e) and (f)). The wave-length increases as the plasma density decreases. Because the wave-length is comparable to the width of the plasma, coherent waves are not observed in the lower density case.

The relation between the wave length and plasma density is discussed in the following. The dispersion relation in a cold plasma with single ion species and electron is written for an ICRF fast wave as

$$N_f^2 \simeq \frac{\omega_{pi}^2}{\Omega_i^2} \frac{1}{1 + \cos^2\vartheta}, \tag{15}$$

where ϑ is the angle between refractive index N_f and the magnetic field directions [6]. Then the wave length, λ, is obtained from Eq. (15) as

$$\lambda \simeq \frac{2\pi Bc}{\omega}\left(\frac{\epsilon_0(1+\cos^2\vartheta)}{m_i n_i}\right)^{1/2}. \tag{16}$$

Although a plasma with two ion species is assumed, Eq. (16) is valid for the low minority ion ratio. In this analysis, only the plasma density n_i is changed. Therefore, $\lambda \propto n_0^{-1/2}$. In Fig. 2, we can see that λ is almost proportional to $n_0^{-1/2}$.

Figure 3 shows the results with $n_{\varphi 0} = 8$ and $f_{\mathrm{RF}} = 42$ (left), 45 (center), and 48 MHz (right). The other parameters are the same as in the case of Fig. 1. Since the wave frequency increases from 42.0 to 48.0 MHz, the ion cyclotron resonance layer and two-ion-hybrid layers shift toward the higher magnetic field side (left side). Therefore, the absorption region moves from 4.25 (Fig. 3-(a)) to 4.0 m (Fig. 3-(b)) and 3.75 m (Fig. 3-(f)). In addition, we can see that the power absorption region shifts to the center region in the averaged minor radius as the wave frequency increases.

Figure 4 shows the results obtained by varying the minority ion ratio: 2.5% (Figs. 4-(a), (d), and (g)); 5% (the same parameters as those of Fig. 1) (Figs. 4-(b), (e), and (h)); and 10% (Figs. 4-(c), (f), and (i)). The other parameters are the same as in the case of Fig. 1. Increasing the minority ion ratio results in an increase in the width between the ion cyclotron resonance and two-ion-hybrid cut-off layers. In addition, the width between the two-ion-hybrid cut-off and two-ion-hybrid resonance layers increases. It is clearly seen that the power absorption increases at the two-ion-hybrid cut-off layer near the minority ion cyclotron

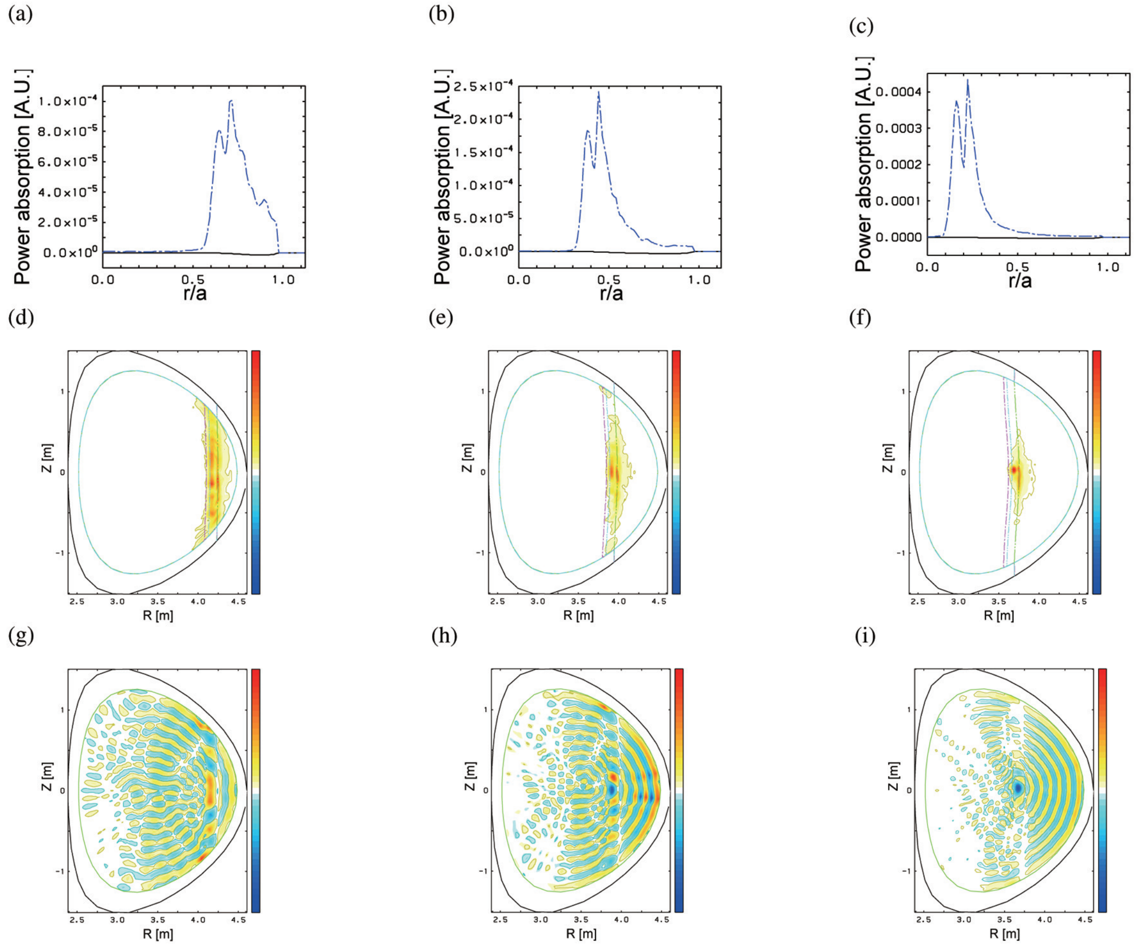

Fig. 3 Wave frequency dependence of the wave propagation and absorption in the minority heating regime of the JT-60U configuration: $f_{\mathrm{RF}} = 42$ (a) and (d); 45 (b) and (e); and 48 MHz (c) and (f). Upper side: minority ion absorption power in the averaged minor radius; middle side: contour plots of minority ion power absorption on the poloidal cross section; and lower side: contour plots of Re E_+ component of the RF electric field. $n_{\varphi 0} = 8$.

resonance layer. As the width between the ion cyclotron resonance and two-ion-hybrid cut-off layers increases, the absorption power near the cut-off layer decreases because of the reduction in the absorption rate.

3.2 Helical configuration (LHD)

We study ICRF minority heating in a helical configuration, taking the LHD plasma as an example. The configuration parameters of LHD are as follows: the plasma major radius $R_0 = 3.6$ m, the plasma minor radius $a = 0.58$ m, and the magnetic field at magnetic axis $B_0 = 2.75$ T.

The wave propagation and absorption are evaluated using TASK/WM with the magnetic flux coordinates obtained using the VMEC code. The used magnetic flux coordinates are shown in Fig. 5, where a vertically elongated cross section is plotted. We assume a configuration with a very low plasma beta (0.01%) for simplicity. The calculation results using TASK/WM for the minority ion heating regime in the LHD plasma are shown in Fig. 6. The assumed plasma parameters are as follows: the temperature at magnetic axis $T_0 = 2.0$ keV, the temperature on plasma boundary $T_s = 0.2$ keV, the density at magnetic axis $n_0 = 0.1 \times 10^{20}\,\mathrm{m}^{-3}$, the density on plasma boundary $n_s = 0.01 \times 10^{20}\,\mathrm{m}^{-3}$, the minority ion ratio 5%, and the ratio of collision frequency to wave frequency $\nu_s = 0.003$. We also assume that antenna current density $j_{\mathrm{ext}} = 1.0\,\mathrm{Am}^{-1}$ and the wave frequency $f_{\mathrm{RF}} = 38.5$ MHz. The temperature and density profiles are set to $T(r/a) = (T_0 - T_s)(1 - (r/a)^2) + T_s$ and $n(r/a) = (n_0 - n_s)(1 - (r/a)^8) + n_s$, respectively. These parameters are based on the typical plasma of ICRF heating experiments in LHD.

The cross sections at various toroidal angles are shown in Figs. 6-(b)~(m), (O: Figs. 6-(b), (f), and (j); 2π Figs. 6-(c), (g), and (k); π Figs. 6-(d), (h), and (l); and $\frac{2}{3}\pi$ Figs. 6-(e), (i) and (m)). The three lines in Figs. 6-(b)~(e) represent the ion cyclotron resonance layer, two-ion-hybrid cut-off layer, and two-ion-hybrid resonance layer outside the torus (right side). Similar to the tokamak case, it is necessary to analyze for ten toroidal wave mode numbers (In helical plasma, $n = n_{\varphi 0} + n'' N_h$, where $n'' =$ integer (n in Eq. (6)), is the toroidal mode number of the waves exited

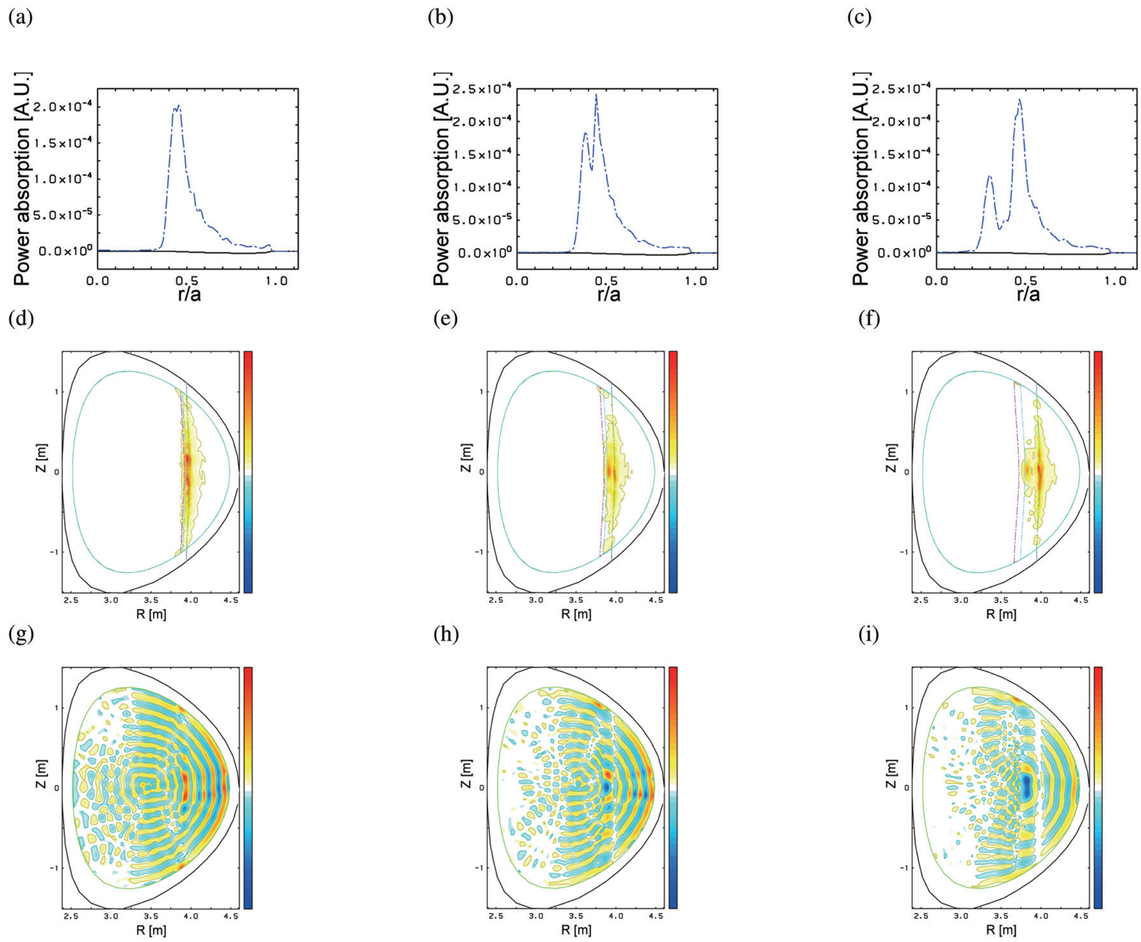

Fig. 4 Minority ion ratio dependence of the wave propagation and absorption in the minority heating regime of the JT-60U configuration: minority ion ratio 2.5% (a), (d), and (g); 5% (b), (e), and (h); and 10% (c), (f), and (i). Upper side: minority ion absorption power in the averaged minor radius; middle side: contour plots of minority ion power absorption on the poloidal cross section; and lower side: contour plots of Re E_{+} component of the RF electric field. $n_{\varphi 0} = 8$.

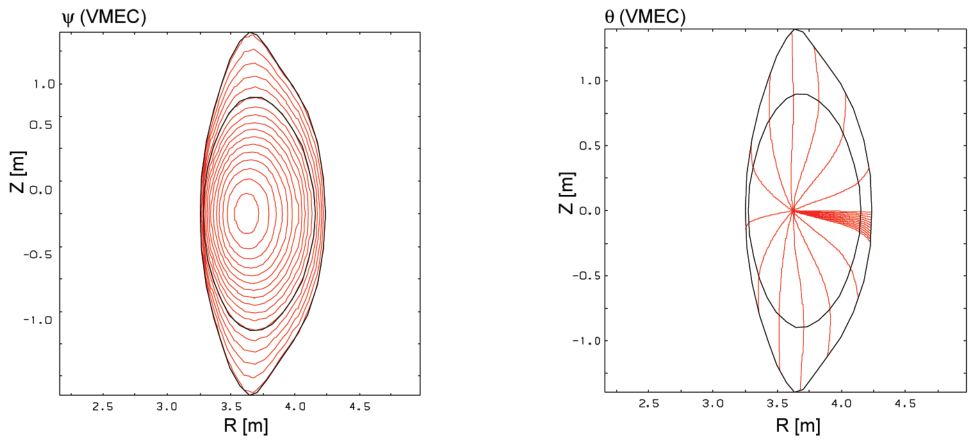

Fig. 5 Contour plots of the magnetic flux coordinates by VMEC, ψ (left), θ (right)

by antenna current) and add their results. Figure 6 is the final results after adding ten toroidal mode results.

It is observed that the absorption region of the minority ions is located near the minority ion cyclotron resonance layer in Figs. 6-(b)~(e), which show similar tendency as those in tokamak plasma. According to Eq. (16), the wave length with this parameter is comparable to that of Figs. 2-(a) and (e). The ion cyclotron resonance and two-ion-hybrid layers are complicated because of the complexity of the magnetic configuration of LHD. Then, the

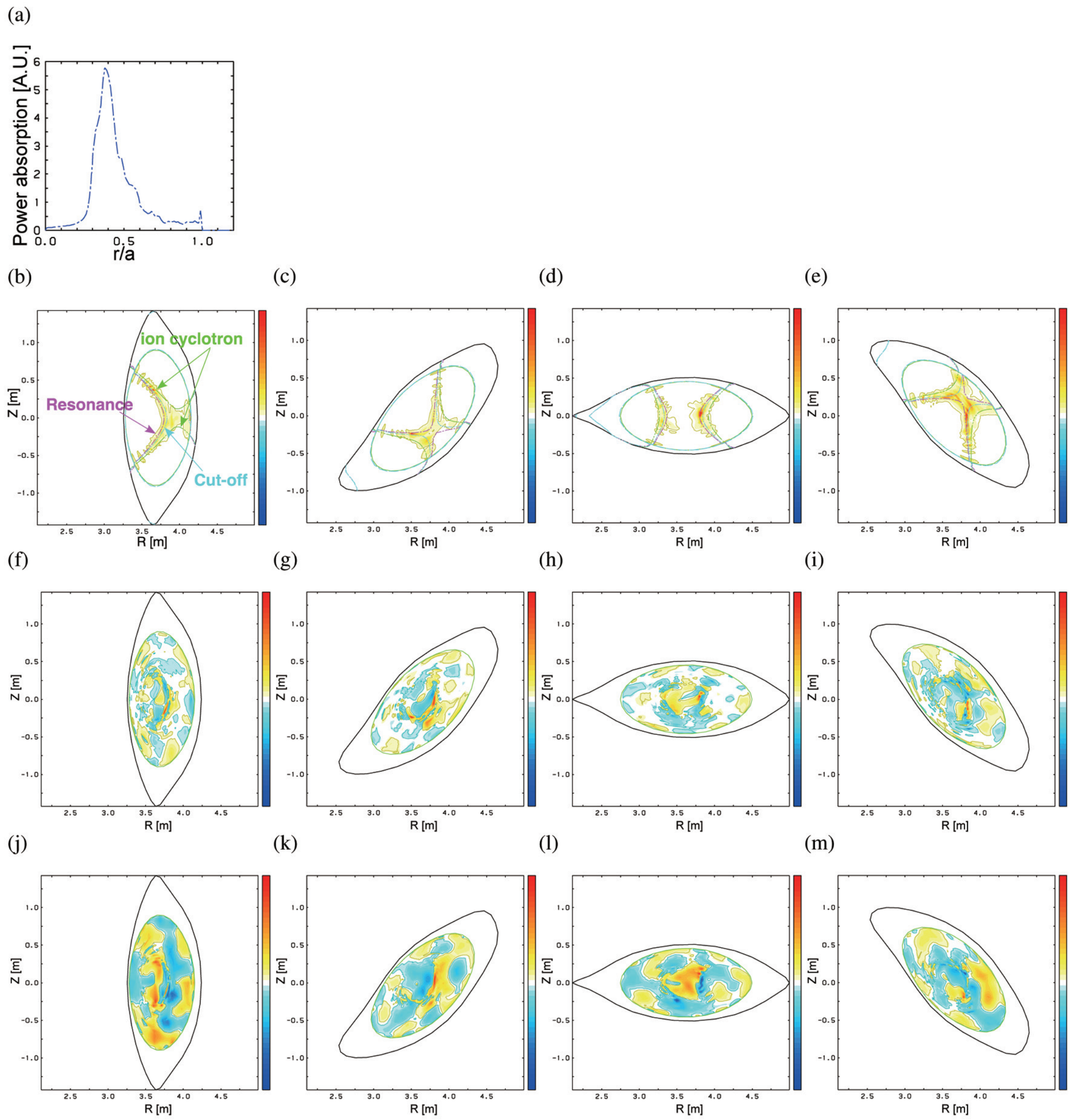

Fig. 6 Wave propagation and absorption in the minority heating regime of the LHD configuration: the minority ion absorption power as a function of the averaged minor radius (a); contour plots of minority ion absorption on the poloidal cross section (b) (e); Re E_+ component of the RF electric field (f) (i); and Re E_- component of the RF electric field (j) (m). $f_{\mathrm{RF}} = 38.5$ MHz.

two-ion-hybrid resonance and two-ion-hybrid cut-off layers exist just at the front of the antenna for the assumed parameters based on the experiment. Therefore, wave propagation direction is not clearly identified in the helical plasma.

Next, we examine the poloidal and toroidal mode number dependences of the calculation results. Although the final result is obtained by adding all the toroidal mode results, we only compare the results with one mode number, $n_{\varphi 0} = 8$, in the followings, because the final result is not much different in tendency from that with one mode. Figure 7 shows results with $n_{\varphi 0} = 8$ and $(l, m, n) = (100, 16, 4)$, while Fig. 6 show results with $(l, m, n) = (100, 32, 8)$, where l, m, n are the number of radial mesh, poloidal mode, and toroidal mode in Eq. (6) respectively. Comparing Fig. 7-(a) to Fig. 6-(a), minority ion (H) absorption distribution of Fig. 7-(a) peaks at the two-ion-hybrid layers unlike that of Fig. 6-(a). In analysis with $(l, m, n) = (100, 16, 4)$, waves at the ion cyclotron resonance and two-ion-hybrid layers can not be expressed because of the lower poloidal and toroidal resolution (Figs. 7-(c) and (d)). Therefore, the analysis with $(l, m, n) = (100, 32, 8)$ is needed to obtain reasonable results.

Next, we study the density dependence of the wave propagation in the LHD configuration. Figure 8 shows results with $n_{\varphi 0} = 8$ and varying density: $n_0 = 0.1 \times 10^{20}\,\mathrm{m}^{-3}$ (Figs. 8-(a) and (e)) (the same parameters as those of Fig. 6); $0.3 \times 10^{20}\,\mathrm{m}^{-3}$ (Figs. 8-(b) and (f)); $0.5 \times 10^{20}\,\mathrm{m}^{-3}$ (Figs. 8-(c) and (g)); and $0.7 \times 10^{20}\,\mathrm{m}^{-3}$ (Figs. 8-(d) and (h)). The other parameters are the same as in the case of

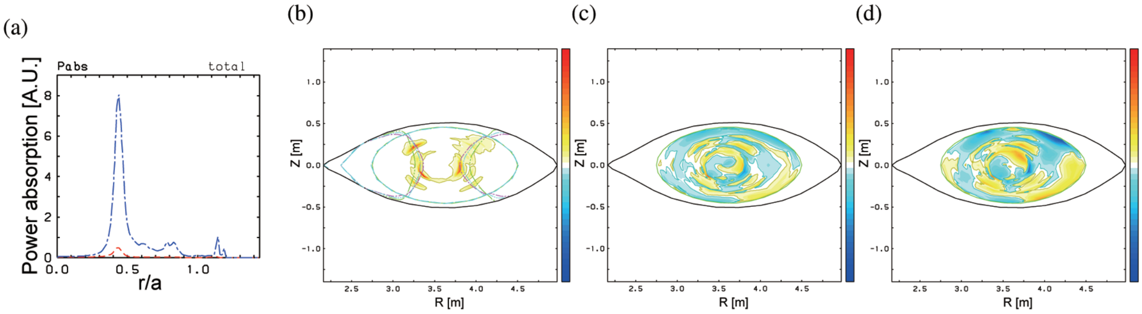

Fig. 7 Poloidal mode number effect on the wave propagation and absorption in the minority heating regime of the LHD configuration: the minority ion absorption power as a function of the averaged minor radius (a); contour plots of minority ion absorption on the poloidal cross section (b); Re E_+ component of the RF electric field (c); and Re E_- component of the RF electric field (d). $(l, m, n) = (100, 16, 4)$ and $n_{\varphi 0} = 8$.

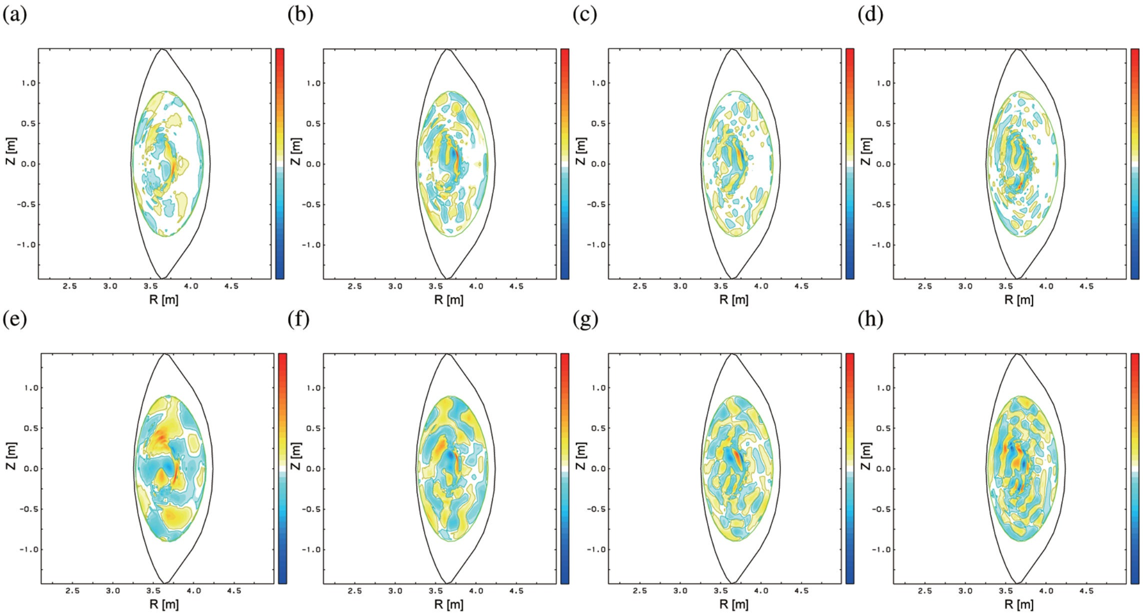

Fig. 8 Plasma density dependence of the wave propagation in the minority heating regime of the LHD configuration: $n_0 = 0.1 \times 10^{20}$ m^{-3} (a) and (e); 0.3×10^{20} m^{-3} (b) and (f); 0.5×10^{20} m^{-3} (c) and (g); and 0.7×10^{20} m^{-3} (d) and (h), Upper side: contour plots of Re E_+ component of the RF electric field on the poloidal cross section and lower side: contour plots of Re E_- component of the RF wave electric field. $n_{\varphi 0} = 8$.

Fig. 6. Re E_+ and Re E_- components of the electric field are shown on the upper and lower sides, respectively, in Fig. 8. It is observed that upen increasing the density, the wave-length decreases and coherent waves are formed.

Figure 9 shows the results with the wave frequency: $f_{\mathrm{RF}} = 36$ (Figs. 9-(a), (e), and (i)); 37 (Figs. 9-(b), (f), and (j)); 38 (Figs. 9-(c), (g), and (k)); and 39 MHz (Figs. 9-(d), (h), and (l)). The other parameters are the same as in the case of Fig. 6. Similar to the tokamak case, the ion cyclotron resonance and two-ion-hybrid layers shift toward the higher magnetic field side, and the absorption region is also shifted because of the increase in the wave frequency.

Figure 10 shows the results with varing minority ion ratio: 2.5% (Figs. 10-(a) and (d)); 5% (the same parameters as those of Fig. 6) (Figs. 10-(b) and (e)); and 7.5% (Figs. 10-(c) and (f)). The other parameters are the same as in the case of Fig. 6. In the case of minority ion ratio 2.5%, it is observed that the wave propagation is little affected by minority ions and the absorption power is lower than that of the 5% and 7.5% cases. On the other hand, in the 5% and 7.5% cases, the wave propagation is strongly affected by minority ions, and the absorption power increases.

4. Conclusions

We have studied ICRF wave propagation and absorption in 3D magnetic configurations using TASK/WM, in which Maxwell's equation for the RF wave electric field is solved as a boundary value problem. We have analyzed the wave propagation and absorption in the tokamak (JT-60U) and helical (LHD) configurations in the minority ion heating regime, assuming a cold plasma dispersion relation. The magnetic flux coordinates based on MHD equi-

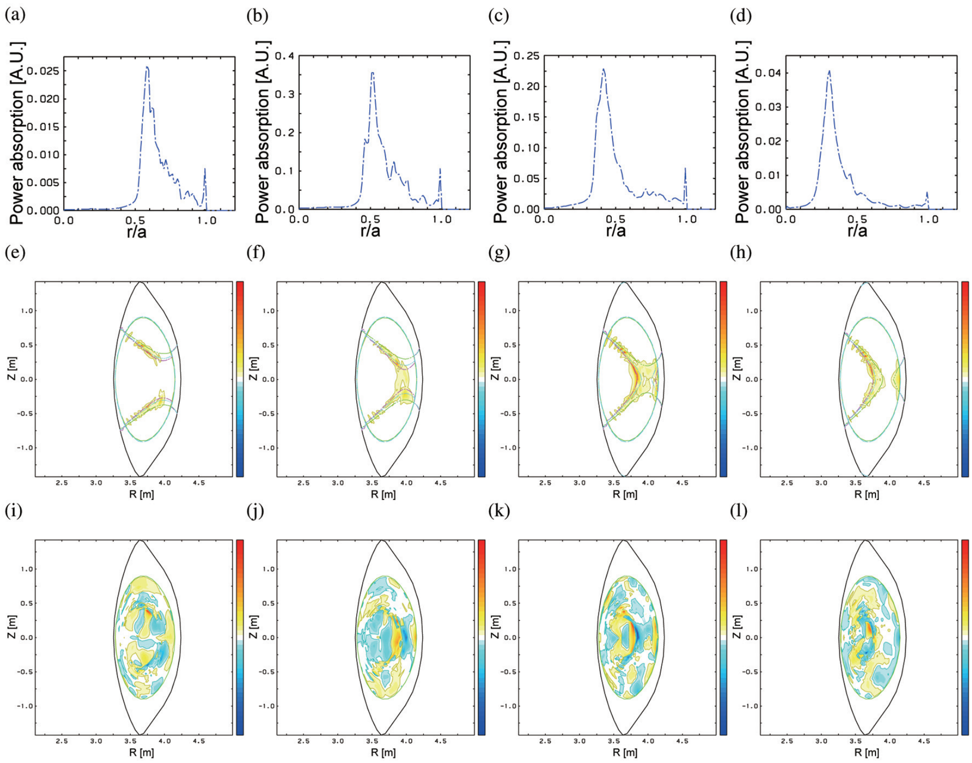

Fig. 9 Wave frequency dependence of the wave propagation and absorption in the minority heating regime of the JT-60U configuration: $f_{\mathrm{RF}} = 36$ (a), (e), and (i); 37 (b), (f), and (j); 38 (c), (g), and (k); and 39 MHz (d), (h), and (l). Upper side: minority ion absorption power in the averaged minor radius; middle side: contour plots of minority ion power absorption on the poloidal cross section; and lower side: contour plots of Re E_+ component of the RF electric field. $n_{\varphi 0} = 8$.

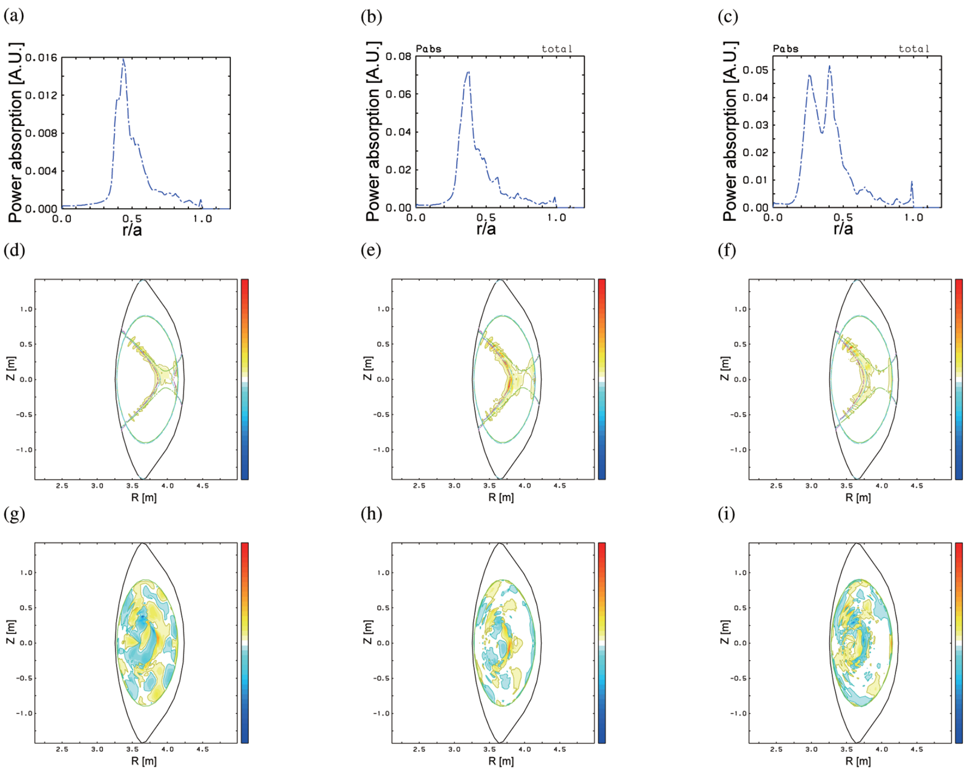

Fig. 10 Minority ion ratio dependence of the wave propagation and absorption in the minority heating regime of the LHD configuration: minority ion ratio 2.5% (a), (d), and (g); 5% (b), (e), and (h); and 7.5% (c), (f), and (i). Upper side: minority ion absorption power in the averaged minor radius; middle side: contour plots of minority ion power absorption on the poloidal cross section; and lower side: contour plots of Re E_+ component of the RF electric field. $n_{\varphi 0} = 8$.

librium in LHD were obtained using the VMEC code. An improved model was applied to the magnetic flux coordinate construction extending to the vacuum region. This model has improved the numerical error near the plasma-vacuum boundary. In addition, a large mode size simulation has been performed. This darifies the wave propagation and absorption at the ion cyclotron resonance and two-ion-hybrid layers in LHD.

The obtained results have shown that the ICRF wave was absorbed at the region near the ion cyclotron resonance, two-ion-hybrid cut-off, and two-ion-hybrid resonance layers in LHD. Both the results in tokamak and helical plasmas have shown a similar tendency in the absorption profiles. However, the ion cyclotron resonance and two-ion-hybrid layers are complicated because of the complexity of magnetic configuration in LHD. Further, the two-ion-hybrid resonance and two-ion-hybrid cut-off layers exist just at the front of the antenna for the assumed parameters based on the experiment. Therefore, the wave propagation direction was not clearly identified in the helical plasma.

In this study, we have assumed a cold plasma dispersion relation, but a dispersion relation including the finite Larmor radius effects is necessary for analyzing higher harmonics heating. The analysis using TASK/WM including these effects will be presented in the future.

[1] T. Mutoh *et al.*, Nucl. Fusion **47**, 1250 (2007).
[2] S. Murakami *et al.*, Nucl. Fusion **46**, S425 (2006).
[3] A. Fukuyama *et al.*, *Proc. 18th Int. Conf. Fusion Energy 2000* THP2-26.
[4] A. Fukuyama and T. Akutsu *Proc. 19th Int. Conf. on Fusion Energy 2002* THP3-14.
[5] T. Seki *et al.*, *16th Topical Conf. on RF Power in Plasmas 2005, AIP Conf. Proc.* **787**, 98.
[6] T.H. Stix, *WAVES IN PLASMAS* (Springer-Verlag New York, Inc. 1992).